CT-Scan study of crack patterns of fiber-reinforced concrete loaded monotonically and under low-cycle fatigue

Miguel A. Vicente, Gonzalo Ruiz, Dorys C. González, Jesús Mínguez, Manuel Tarifa, Xiaoxin Zhang

PII: S0142-1123(18)30182-8
DOI: https://doi.org/10.1016/j.ijfatigue.2018.05.011
Reference: JIJF 4683

To appear in: *International Journal of Fatigue*

Received Date: 10 March 2018
Revised Date: 7 May 2018
Accepted Date: 9 May 2018

Please cite this article as: Vicente, M.A., Ruiz, G., González, D.C., Mínguez, J., Tarifa, M., Zhang, X., CT-Scan study of crack patterns of fiber-reinforced concrete loaded monotonically and under low-cycle fatigue, *International Journal of Fatigue* (2018), doi: https://doi.org/10.1016/j.ijfatigue.2018.05.011

CT-Scan study of crack patterns of fiber-reinforced concrete loaded monotonically and under low-cycle fatigue

Miguel A. Vicente[a,b], Gonzalo Ruiz[c,*], Dorys C. González[a,b], Jesús Mínguez[a], Manuel Tarifa[d], Xiaoxin Zhang[c]

[a] *E. Politécnica Superior, Universidad de Burgos, Campus Milanera (Edif. D); c/ Villadiego s/n, 09001 Burgos, Spain*
[b] *Parks College of Engineering, Aviation & Technology, Saint Louis University, 3450 Lindell Blvd, 63103 Saint Louis, MO, USA*
[c] *ETSI de Ingenieros de Caminos, C. y P., Universidad de Castilla-La Mancha, Avda. Camilo José Cela s/n, 13071 Ciudad Real, Spain*
[d] *E.I. Minera e Industrial de Almadén, Universidad de Castilla-La Mancha, Plaza de Manuel Meca 1, 13400 Almadén, Spain*

Abstract

Most fatigue models for concrete under compression assume, as an axiom, that compressive tests are a limit case for a cyclic test where failure is achieved in the first cycle. This is supported by the fact that the crack patterns obtained in both cases are similar to the naked eye. This paper focuses on verifying whether this observation is correct or not. For that, we used a Computed Tomography Scan together with digital image processing to obtain 3D damage maps of tested 40 mm edge-length cubes made of steel fiber-reinforced concrete. The cubes were classified in series according to the type of loading: intact, monotonic and cyclic. They were scanned to acquire their 3D damage maps. Additionally, a specific post-processing algorithm was developed by the authors to compare the different crack patterns. The results show that average damage maps for monotonically and cyclically-tested cubes are statistically similar, thereby confirming the initial hypothesis for steel fiber-reinforced concrete. Furthermore, damage distribution near the platens apparently depends on whether it is a fixed platen or it is adjustable to the specimen surface due to a spherical seat.

*Corresponding author
Email address: Gonzalo.Ruiz@uclm.es (Gonzalo Ruiz)

Keywords: Fatigue of steel fiber-reinforced concrete, CT-Scan, digital image processing, 3D crack pattern.

1. Introduction

In recent years, the increased strength of concretes and the greater use of slender structural elements have focused attention on the development of fatigue models. These models associate the cyclic loads, which in fact have become the main loads on structures in many cases, with a fatigue life prediction. Most models are deterministic [1, 2, 3, 4, 5], whereas others include the probabilistic nature of the failure in their formulations [6, 7, 8]. For example, Saucedo *et al*. [8] developed a fatigue model for concrete that takes into account the statistical distribution of the strength data.

In addition, it is commonly assumed, as an axiom, the hypothesis that quasi-static monotonic tests are a limit case of cyclic tests where failure is achieved in the first cycle (also called hypothesis of convergence to the *initial distribution* [8], that is the probabilistic distribution of a series of monotonic tests). This hypothesis is not exclusive for concrete, since it is also considered, in an implicit way, in many other materials. Indeed, previous research suggests that low and medium-cycle fatigue results can be fitted by a linear relation between the relative maximum stress level, S, and the logarithm of the number of cycles, N, i.e. by $S = A - B \log N$, where A and B are fitting coefficients. The aforementioned axiom should imply that A be equal to one, but this may not be the case, which would mean that this fit does not converge to the monotonic tests, i.e. fatigue and monotonic behaviors are different physical phenomena and they should be predicted using various types of equations that do not converge to the monotonic case [9, 10, 11, 12, 13, 14, 15, 16].

However, after the research carried out by Ass-Jakobsen [1] and Tepfers and Kutti [2], almost all the research works on concrete have used the expression $S = 1 - B \log N$, with the aim of including the hypothesis of convergence to the initial distribution ($N = 1$ and $S = 1$). Moreover, international standards

define S-N curves according to this criterion [17, 18]. This way of approaching and understanding the fatigue behavior of concrete under compressive cyclic loads implicitly assumes that the failure internal micro-mechanisms in concrete (crack nucleation and growth, crack distribution, etc.) due to monotonic static compressive tests are almost identical to the ones due to low-cycle compressive fatigue tests. This hypothesis is basically supported by the fact that the crack patterns obtained in both cases are similar to the naked eye. Still, the extension of the damage propagation or even some fracture mechanisms could vary with the type of loading. Moreover, such variations could leave a trace in the internal cracking pattern and thus could be studied with a Computed Tomography Scan (CT-Scan) equipment combined with a data processing technique that could provide a more solid statistical evidence than just a qualitative comparison between a few tested specimens. However, no further analyses of the crack patterns in monotonically and cyclically loaded specimens have been conducted. Precisely this is the objective of this research, that is to verify the initial-distribution hypothesis using CT-Scan technology combined with a specific post-processing software specifically developed for this work.

The CT-Scan is a non-destructive technique which currently is being used widely to study the microstructure of materials. This technology is able to define the density of each specimen voxel (volumetric pixel) by assigning a shade of gray according to voxel density. Light shades of grey correspond to high densities, whereas dark shades of grey correspond to low densities. In recent years, many authors have conducted research on the concrete microstructure through this technique, in particular, many have focused on the fiber-orientation and fiber-distribution inside a concrete matrix [19, 20, 21, 22, 23, 24, 25, 26, 27]. Some other research works have been focused on the spatial distribution of concrete voids and its effect on macroscopic properties [28, 29, 30, 31, 32, 33, 34, 35]. A complete state-of-the-art on the use of computed tomography to explore the microstructure of materials in civil and mechanical engineering, is exposed in Vicente *et al.* [36].

In this paper, the CT-Scan is used in order to detect the voids inside the

material —a self-compacting fiber reinforced concrete— which are either voids of a pre-existing pore or those making up a newly formed crack. The specimens were classified into series according to the type of loading: intact, monotonic and cyclic; series of specimens were large enough to be statistically representative of each loading case. Apart from the beneficial effect of fibers in enlarging the fatigue life [8, 37, 38], they also give enough cohesion to specimens to avoid comminution after being tested. All the specimens were scanned in order to determine their 3D crack maps and to compare the type of damage generated by each type of loading. The images were processed with a novel methodology, specifically developed by the authors for this research, which sums the voxels representing voids along the height or along circumferences around the loading direction, to generate average histograms that allow quantitative comparison among them. Additionally, the images of intact specimens were used to check that the specimen making process led to a similar fiber disposition across the specimens. The results show a similar crack pattern in the monotonically and cyclically-loaded specimens, which confirms the hypothesis of convergence to the initial distribution. Moreover, our specific post-processing methodology allows to detect a non-uniform distribution of cracks along the height of the specimens which apparently follows from the boundary conditions of the tests.

This paper is structured as follows: The experimental procedure is presented in Section 2, the results of the tests are described and discussed in Section 3; and finally the conclusions are found in Section 4.

2. Experimental procedure

In this section, the materials, the experimental procedure and the scanning procedure are described.

2.1. Material characterization

Cubic specimens from a single self-compacting concrete made of a siliceous aggregate of 8 mm maximum size and CEM I 52.5 SR cement were used throughout the experiments. The mixing proportions by weight were: $1 : 0.32 : 2.25 : 1.73 :$

0.44 : 0.012 (cement : filler : sand : coarse aggregate : water : superplasticizer). The concrete was reinforced with 15 kg/m^3 of steel-fibers, i. e. concrete had a fiber volume fraction of 0.2%. Fibers were 13 mm in length and 0.21 mm in diameter, which results in an aspect ratio of 62. Their tensile strength was 2750 MPa and their modulus of elasticity was 200 GPa, as specified by the maker (which is Bekaert; the commercial name of this type of fiber is Dramix® OL 13/.20). As concrete was self-compacting, the segregation of fibers due to vibration was avoided [39].

The cubes were 40 mm in edge length and were cut from prisms of 100×100 mm^2 in cross-section and 420 mm in total length, with a tolerance of ± 0.2 mm. The molds were filled from the center so that the mix flowed along them. Once the prisms hardened, they were cut into nine slices, each slice was cut into two small prisms and from each of them, again by cutting, two cubes were obtained. Even though just one prism produces 36 cubes, the cubes in this research came from nine identical prisms from the same batch, since we were also producing cubes for other experimental programs [40, 41]. All the faces of the cubes were ground to the prescribed dimensions, accounting for the fixed tolerance (± 0.2 mm). This process was done so that the cubes were obtained from the core of the original prism, thus avoiding the wall effect, i. e. preferential fiber alignment and concentration near the specimen faces in contact with the mold. Figure 1 illustrates the process.

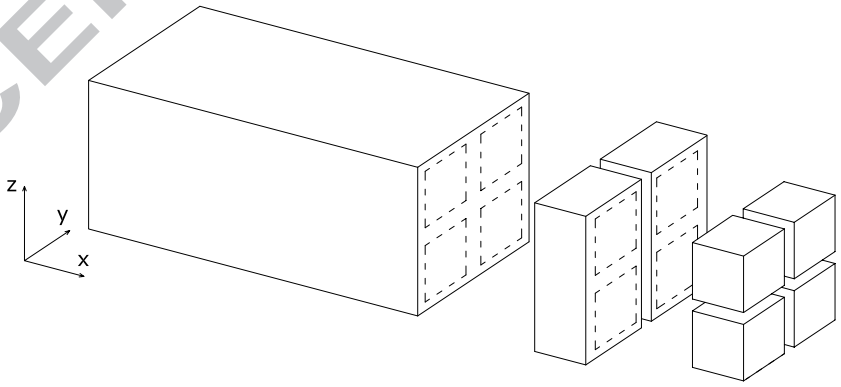

Figure 1: Procedure to obtain the cubes from prisms.

All the cubes were labeled so that they could be identified later on. The label was glued to one of the lateral faces so that the direction of casting (z-axis) was always known. Cubes were always tested along this direction, i. e. the casting direction coincided with the loading axis. We did not keep track of the other two cartesian coordinates because we assumed that there were not going to be significant differences in the fiber orientation with respect to them. This assumption was checked later on by identifying all the fibers in a series of intact cubes and by measuring their corresponding angles in the spherical coordinate system (see section 3.1).

The concrete compressive strength f_c was 55.7 MPa with a standard deviation of 2.1 MPa, obtained from 12 cubes tested at a loading rate of 0.3 MPa/s, see Table 1. Furthermore, the stress–strain curves of the 12 monotonic compressive tests are represented in Fig. 2. The elastic modulus E was 20.4 GPa with a standard deviation of 1.0 GPa. It was measured by adapting the standard procedure described in EN12390-13 [42] to 45×45×90 mm^3 prisms, as shown in Fig. 3. The mean density ρ was 2334 kg/m^3 with a standard deviation of 23 kg/m^3.

Table 1: Compressive strength from the cubes tested in monotonic compression.

Specimen	f_c (MPa)	Specimen	f_c (MPa)
1c	54.7	7c	55.4
2c	52.7	8c	52.6
3c	57.1	9c	58.9
4c	54.2	10c	56.3
5c	57.8	11c	57.5
6c	54.0	12c	57.2
Mean	55.7	Std. dev.	2.1

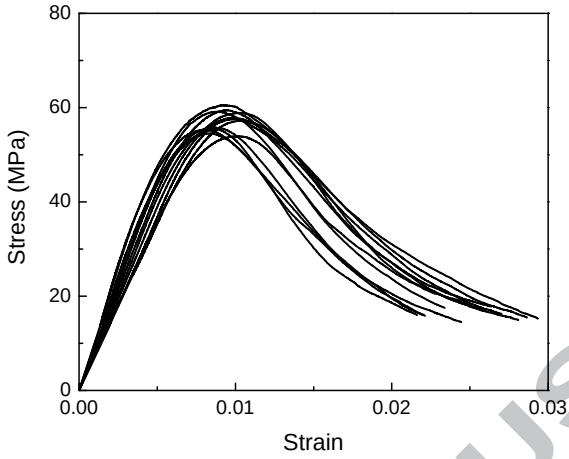

Figure 2: Stress-strain curves of the cubes tested in monotonic compression.

The concrete cubes were divided into three series as follows. The cyclic series consisted of 16 specimens tested under low-cycle fatigue loading, the monotonic series were 8 of the specimens tested under monotonic compressive loading and the intact series were another 8 cubes, taken at random, which were scanned in order to get the fiber and the void distribution within the concrete before being tested.

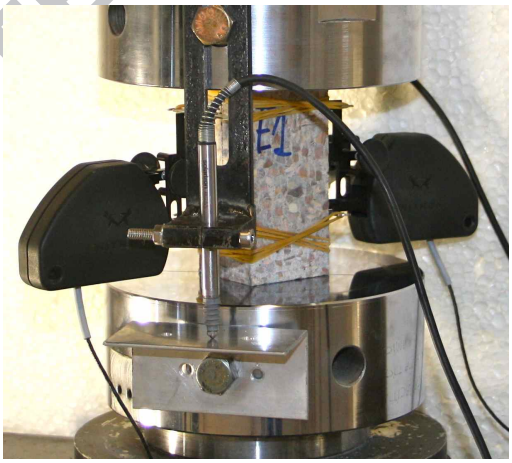

Figure 3: Experimental set-up to measure the elastic modulus.

2.2. Fatigue tests performed

Compressive fatigue tests (cyclic loads) were performed on the specimens of the cyclic series. The tests were carried out at a loading frequency of 10 Hz under sinusoidal stress cycles varying between a minimum of $0.34\,f_c$ and a maximum of $0.83\,f_c$. The number of cycles resisted by each specimen is shown in Table 2. According to Model Code 2010 [17], the expected fatigue life is 10^3 cycles, so they can be considered as low-cycle fatigue tests.

All the tests were conducted in a servo-hydraulic machine with a maximum loading capacity of 250 kN. The machine was equipped with two compressive steel platens and a spherical seat in the upper part in order to align the load, see Fig. 4. The tests were preceded by a pre-load of 4 kN in order to adjust and to fix the spherical seat.

Table 2: Specimens tested under cyclic loads (Cyclic series).

Cycles for $\sigma_{max} = 0.83\,f_c$; $\sigma_{min} = 0.34\,f_c$			
Specimen	Cycles	Specimen	Cycles
$1f$	1312	$9f$	2651
$2f$	12065	$10f$	97
$3f$	435	$11f$	68
$4f$	1934	$12f$	47046
$5f$	150	$13f$	46
$6f$	841	$14f$	6858
$7f$	39	$15f$	4493
$8f$	2070	$16f$	1143

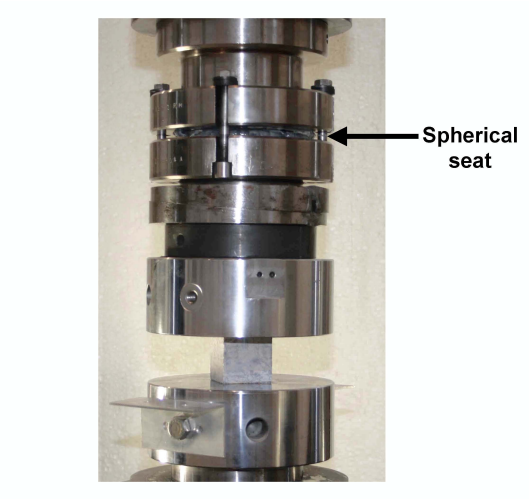

Figure 4: Experimental set-up for the fatigue tests.

2.3. Scanning of the specimens

Once the specimens had been tested under monotonic or cyclic loads, they were scanned by using a CT-Scan. A total of 32 scannings of specimens were performed.

The CT-Scan used was a GE Phoenix v|tome|x device of the *Centro Nacional de Investigación sobre la Evolución Humana*, Burgos, Spain. It is equipped with a tube of 300 kV/500 W. The CT-Scan has a post-processing software which provides flat pictures of 2048×2048 pixels. Thus, for a section of 40×40 mm^2, the equipment provides a horizontal resolution of 30×30 μm^2. The vertical distance between the cutting planes was fixed in 30 μm, so the CT-Scan produced 1334 pictures per specimen, such as the one shown in Fig. 5. The scanner assigns a shade of gray according to the voxel density. Light shades of grey signify high densities and dark shades of grey signify low densities.

The result of the scanning is a dot matrix containing the cartesian coordinates x, y and z of the center of gravity of the voxels according to their density. The total number of voxels in a specimen are approximately 2.4×10^9.

The post-processing software identifies empty voxels or, that is, voxels with

a density equal to both voids or cracks, in order to generate a 3D image of the specimen damage, see Fig. 6. We also identified all the fibers in the cubes of the intact series from voxels whose density is equal to that of steel, see Fig. 7. Apparently, fibers tend to be perpendicular to the z-axis while they do not show any preferential orientation with respect to the other two axes. However, this observation corresponds to a single cube and, thus, it should be backed by a complete analysis of the whole series. To do that we used a software called OPTIFIBER, developed by Vicente et al. and described in [23], which measured and aggregated the angles of all the fibers with respect to the coordinate axes. Histograms corresponding to this study on fiber distribution and orientation are presented in section 3.1.

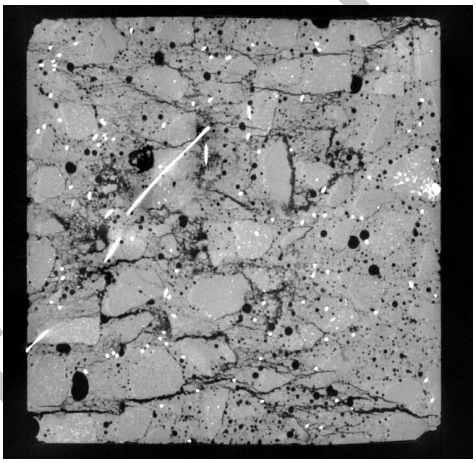

Figure 5: CT-Scan picture.

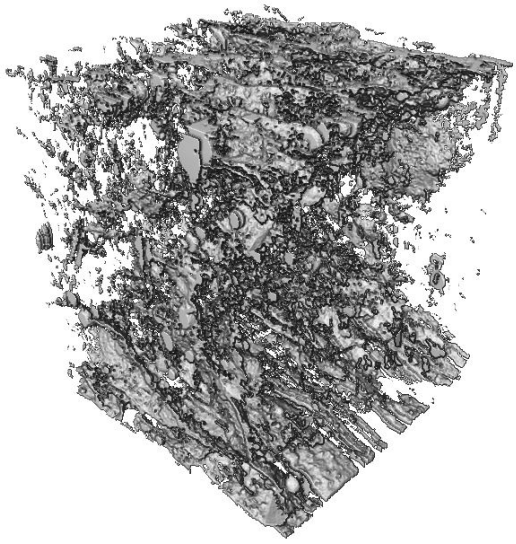

Figure 6: 3D image of empty voxels within a specimen obtained with the CT-Scan.

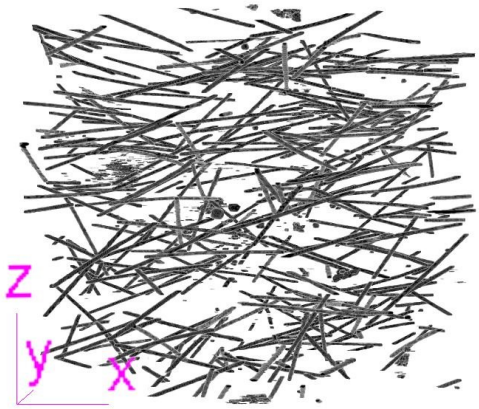

Figure 7: Fiber distribution in one of the specimens of the intact series.

The empty volume per specimen in every series is set forth in Table 3. In the case of the intact series, empty volume corresponds only to voids, while for the monotonic and cyclic series, empty volume corresponds to both, that is

voids and cracks together, which cannot be differentiated. An analysis of the information in Table 3, firstly demonstrates the empty volume in the intact series is much lower than the one in the monotonic and cyclic series. Secondly, the monotonic series shows a similar empty volume than the cyclic series, but a lower standard deviation.

Table 3: Empty volume per specimen in every series.

Specimen	Empty volume (mm^3)		
	Intact	Monotonic	Cyclic
1	1588	2616	2648
2	1573	2803	3047
3	1610	2697	4407
4	889	2588	2844
5	916	2484	3646
6	1912	2351	2015
7	1411	2253	2886
8	1503	2719	2642
9	–	–	2090
10	–	–	4042
11	–	–	3091
12	–	–	3422
13	–	–	3256
14	–	–	2786
15	–	–	2976
16	–	–	1738
Mean volume	1425	2564	2971
Std. dev.	353	189	705
Mean percentage	2.2	4.0	4.6
Std. dev.	0.6	0.3	1.1

Neither direct analysis of the 3D images generated by the CT-Scan nor the comparison of the average empty volumes allows defining the crack patterns. Therefore, an analysis procedure, referred to as a *circumferential test*, was de-

veloped in order to find a numerical criterion to quantify the extent of the damage within the specimen.

2.4. Circumferential test

In this section we describe the circumferential test, which is the procedure for analyzing the raw data from the CT-Scan in order to disclose the extent of damage generated in the mechanical tests.

The steps for analyzing the data are as follows:

(1) First, the voxel coordinates x_i and y_i (taken with respect to one of the vertices of the cube, the axes aligned along the three edges converging on it; the z axis is always parallel to the loading direction) are normalized between 0 and 2 for the x and y direction, and the coordinate z_i is normalized between 0 and 1 for the z direction by means of the following equations:

$$x_{rel} = \frac{2\,x_i}{x_{max}} \qquad y_{rel} = \frac{2\,y_i}{y_{max}} \qquad z_{rel} = \frac{z_i}{z_{max}} \tag{1}$$

where x_{max}, y_{max} and z_{max} are the total dimensions of each cube.

(2) Each voxel is identified by a pair of coordinates, the distance of the voxel to the center of gravity of the cross-section d, which ranges from 0 to $\sqrt{2}$, and height of this cross-section h which ranges from 0 to 1, see Fig. 8. For that, the following equations are used:

$$d = \sqrt{(x_{rel} - x_{G,rel})^2 + (y_{rel} - y_{G,rel})^2} \qquad h = z_{rel} \tag{2}$$

where $x_{G,rel}$ and $y_{G,rel}$ are the normalized coordinates of the center of gravity of the considered section (they should be approximately equal to 1 when accounting for the tolerances in the cube dimensions).

(3) The cube coordinates d and h are divided into twenty subdivisions each, so that the voxels are clustered for all the combinations of d and h coordinates. Thus, the whole cube volume is divided into 400 sub-volumes. For each, we calculate the relative frequency of occurrence of empty voxels

with the following equation:

$$\text{R. frequency} = \frac{N_i}{N_t} \tag{3}$$

where N_i is the number of empty voxels found in the sub-volume and N_t is the total number of empty voxels of the complete specimen.

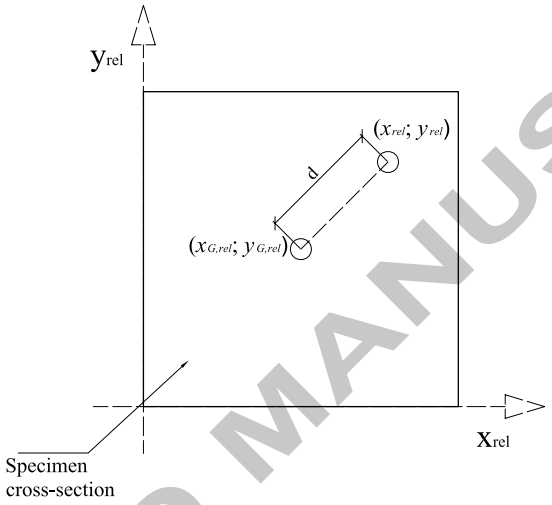

Figure 8: Voxel coordinates.

Additionally, a random defect distribution, inside a theoretical 40 mm edge-length specimen, was simulated through a Monte Carlo statistical model of 10^6 points. The random distribution was used to indicate the randomness of cracks and voids in the studied series. It is also possible to derive analytic functions for a random distribution of voids, but we preferred to use the Monte Carlo simulation because it allows a direct check that the post-processing algorithms provide accurate results, especially when voids in voxels close to the surfaces and to the edges of the cube are analyzed.

Note that the circumferential test sums the frequencies of occurrence around the loading axis, since each sub-volume is similar to the part within the cube of a ring with a rectangular section. It is assumed that this information is relevant even for specimens that are not axi-symmetrical such as for cubes.

3. Results and discussion

In this section, the results of the CT-Scan are shown. Firstly, the results on the fiber distribution are presented. Secondly the results on the void distribution are presented by means of the 3D histograms of each specimen. Finally, the results are combined in 2D histograms in the d direction first and in the h direction subsequently, in order to be analyzed appropriately.

3.1. Fiber distribution and orientation

As mentioned before, it was assumed that the flow of the fresh mix along the mold could lead to fiber orientation, which lead to identify the casting direction as the z-axis and to load all the cubes along it. We did not expect significant differences with respect to x and y-axes and, thus, we did not consider it necessary to mark the other two directions. This assumption was checked by identifying all the fibers in the cubes of the intact series and by measuring the corresponding angles of the fibers in the spherical coordinate system. Fig. 7 shows the image obtained for one of the cubes. It seems that fibers tend to be perpendicular to the z-axis in the average while they are randomly oriented in the horizontal plane. This observation is confirmed by histograms that aggregate the results from the eight cubes of the series for the angle of fibers with the z-axis (θ; see Fig. 9) and for the angle of the projection of the fibers on the horizontal plane with the x-axis (φ; see Fig. 10). The cube in Fig. 7 is represented as '1n' in Figs. 9 and 10.

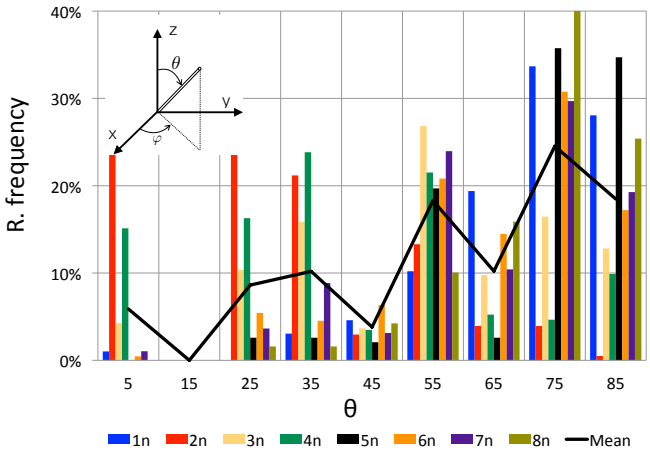

Figure 9: Fiber orientation with respect to the θ angle.

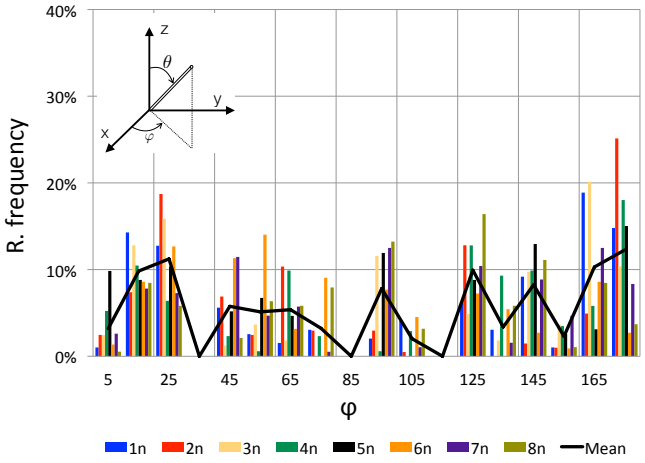

Figure 10: Fiber orientation with respect to the φ angle.

The columns in these histograms represent the relative frequencies of fibers within a range of angles. Frequencies of occurrence are taken relative to the total number of fibers in each cube (which were around 270 fibers per cube). For instance, Fig. 9 shows eight columns in the range between 70° and 80°;

each column corresponds to the number of fibers whose θ angle (i. e. angle with respect to z-axis) is between 70° and 80° divided by the total number of fibers in a single cube. The average of the eight cubes is almost 25%, as can be seen in the plot. All the average points are united by straight segments to form the average line, which shows an increasing trend towards 90°. This indicates that fibers tend to align perpendicularly to the casting direction, presumably because of the flow of the mix while the mold is being filled, as initially assumed. Contrariwise, the histogram that correspond to the φ angle (i. e. angle of the horizontal projection of the fiber with respect to the x-axis) shows that there is no preferential orientation within horizontal planes, since the average curve —albeit rather jagged— does not show fiber concentrations at any angle.

The above study allows concluding that there should not be significant differences among the crack patterns due to the fiber distribution, since we always loaded the cubes along the casting direction. Fibers tend to lay horizontally with no preferential direction. Thus, the orientation, position and distribution of the fibers are similar in the average in all of the cubes used in this research.

3.2. 3D histograms

The 3D histograms plot the d and h coordinates versus the corresponding relative frequency (R. frequency) of occurrence of empty voxels within the corresponding sub-volume. Note that the probability of occurrence of empty voxels for the sub-volume at $d = 1$ is the highest, as shown in the random histogram of Fig. 11, since such sub-volume corresponds to the longest ring inside the cube.

Fig. 12 shows the histogram of an intact specimen. In this case, there are few empty voxels compared to the tested specimens. Histograms of intact specimens are much less uniform than artificial random ones, since actual pores also have a size distribution that was not simulated. Indeed, the peaks in Fig. 12 represent the presence of large pores within the annular sub-volume. In any case, as expected, the higher peaks are located around $d = 1$.

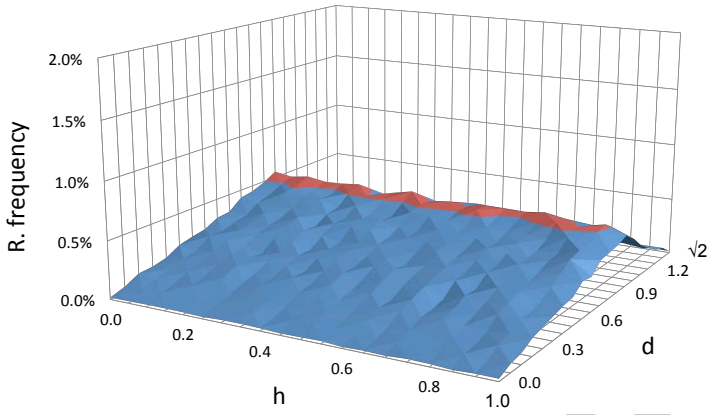

Figure 11: 3D Histogram. Random defects distribution.

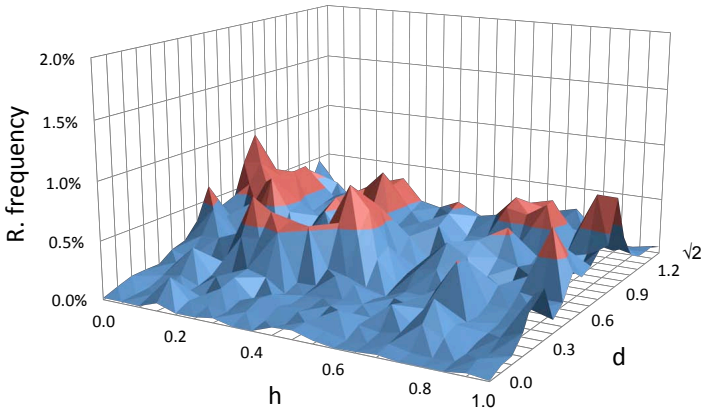

Figure 12: 3D Histogram. Specimen of the intact series.

On the other hand, Fig. 13 shows a monotonically-loaded specimen and Fig. 14 shows a cyclically-loaded specimen. In both cases, there are more empty voxels than in the intact specimens as they correspond to both voids and cracks. Indeed, these histograms basically represent the crack pattern of the corresponding cube. Note that their shape is softer than in the intact series because the total number of empty voxels is much higher. Once again, the relative frequency of occurrence of empty voxels is the highest around $d = 1$.

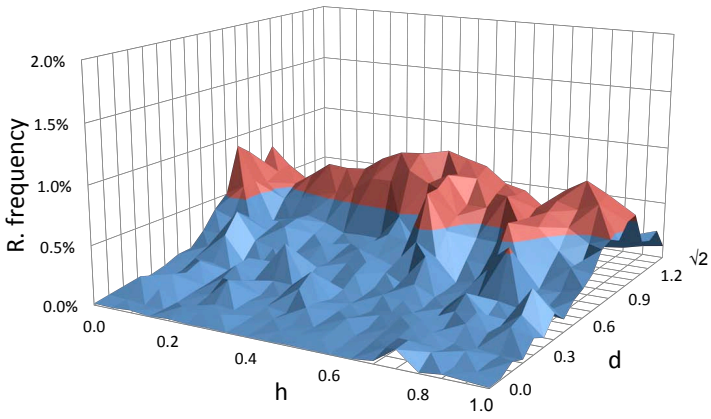

Figure 13: 3D Histogram. Specimen of the monotonic series.

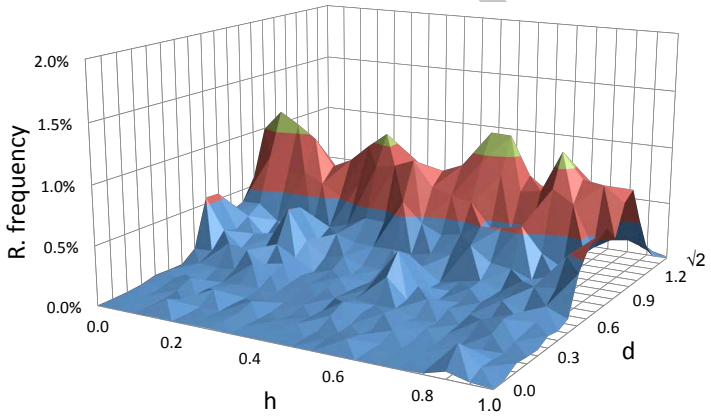

Figure 14: 3D Histogram. Specimen of the cyclic series.

Histograms of the specific cubes of the monotonic and cyclic series may be quite different from each other, even within cubes of the same series, although all of them clearly differ from the histograms of intact specimens or the artificially-generated ones. Comparison between all of the histograms at a glance can be easily performed by combining the frequencies of each of the dimensions of the annular sub-volumes, which yields 2D summed histograms along h and d.

3.3. Summed histograms along the h direction

In order to analyze the results appropriately, the 3D histograms were summed in the h direction, obtaining 2D histograms which represent the relative frequency of occurrence of empty voxels along the d coordinate, or transversal to the load direction.

Fig. 15, 16 and 17 show the summed histograms in the h direction for all the series (intact, monotonic and cyclic). The solid red line shows the mean values obtained from the scanned specimens. All the series were compared with the random curve in black, which represents a random distribution of defects. This comparison follows the concept of statistical significance, which classifies results as significant or not significant based on p values [43]. The p value is the probability that the test hypothesis is true; for example, if a test of the null hypothesis gave $p = 0.01$, the null hypothesis would had only a 1% chance of being true; if instead it gave $p = 0.40$, the null hypothesis would had a 40% chance of being true. In our case, the null hypothesis means similarity in the compared data regarding the p values taken. Thus, we take an upper limit of $p = 0.95$ and a lower limit of $p = 0.05$ and so we have a confidence interval of 90%, which represents the range of values to consider two curves as similar.

On the one hand, the intact series, Fig. 15, shows an almost perfect coincidence between the mean curve and the random one. Thus, it can be said that the defects in the intact series are randomly-distributed, but these defects correspond only to voids in the concrete paste, since this series is only composed of non-tested specimens.

On the other hand, the mean curves of the monotonic and cyclic series, represented by Figs. 16 and 17, are quite different from the random one. This signifies that the damage produced on tested specimens under monotonic or cyclic loads does not follow a random distribution. Furthermore, both series reveal that the relative frequencies in the internal part of the cubes are lower than the corresponding random frequencies. The crossing point between the mean curve and the random one is roughly located at $d = 0.9$. This value divides the cube into two parts: an internal cylinder representing approximately 65%

of the cube volume and the external part formed by the rest of the cube.

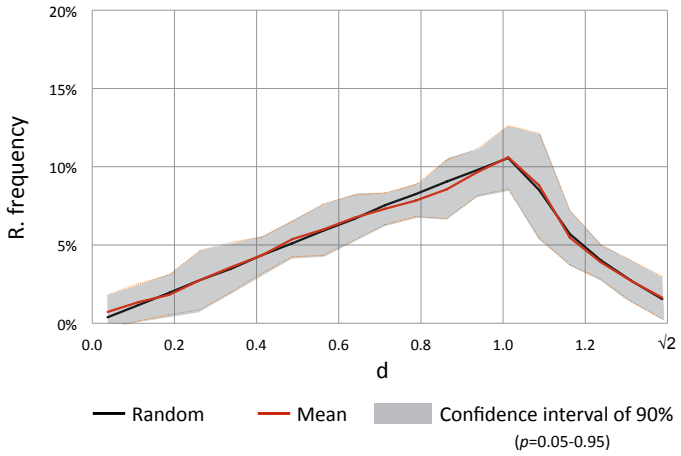

Figure 15: Summed histograms in the h direction. Intact series.

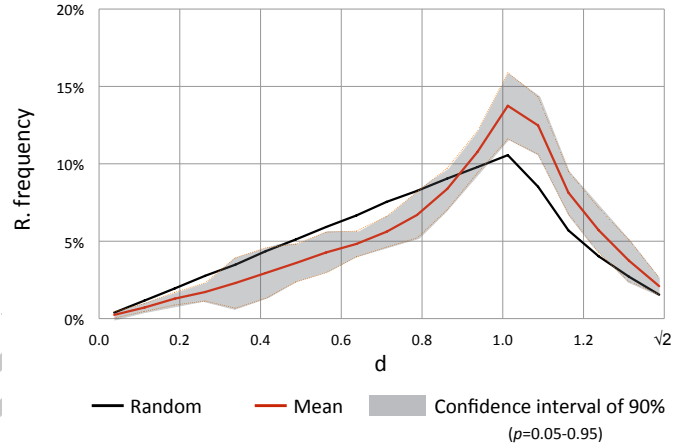

Figure 16: Summed histogram in the h direction. Monotonic series.

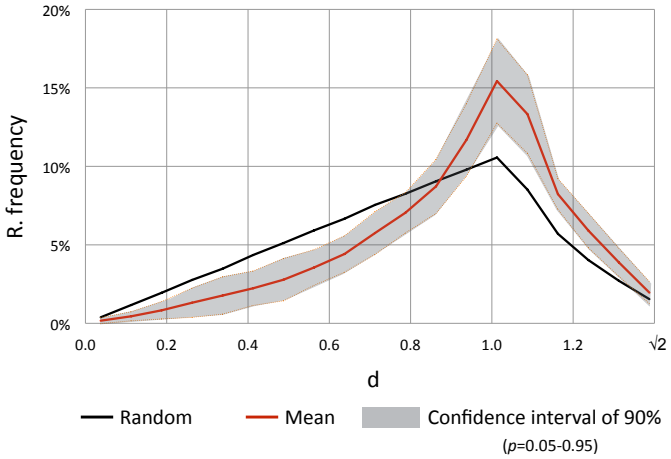

Figure 17: Summed histogram in the h direction. Cyclic series.

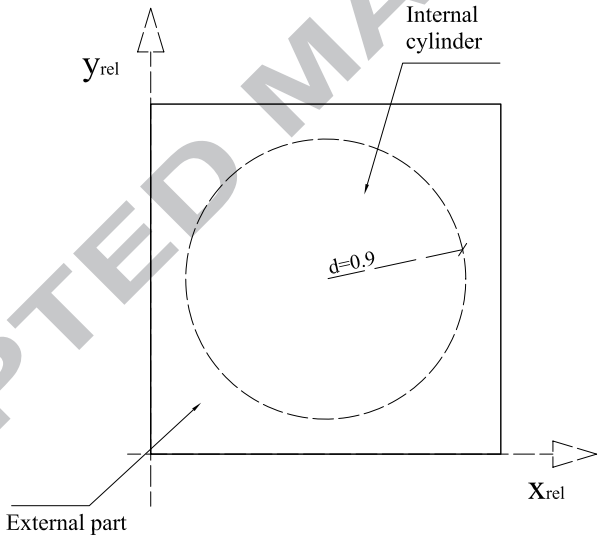

Figure 18: Damage location in the tested specimens.

The comparison between the summed histograms of the monotonic series and the cyclic series is presented in Fig. 19. The curves are quite similar, which means that both, monotonic and cyclic tests, produce a similar crack pattern.

The described results confirm the hypothesis followed by most fatigue models

of convergence to the initial distribution, by which the compressive monotonic test is considered a particular case of the cyclic test, where the number of cycles resisted is only one.

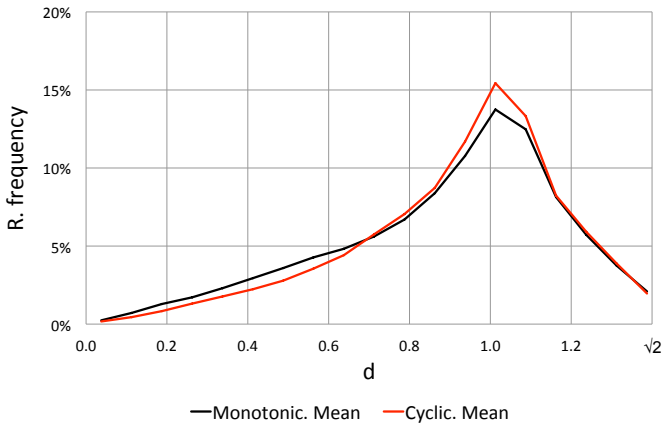

Figure 19: Comparative summed histograms in the h direction. Monotonic and cyclic series.

Additionally, Figs. 20 and 21 show other transversal histograms, where the h coordinate was added by thirds. Therefore the upper third, the central third and the bottom third are represented in order to reveal the effect of the boundary conditions of the tests in the crack pattern. Figures 20 and 21 are comprised of the mean histograms of the monotonic and the cyclic series by thirds; the resulting relative frequencies are multiplied by three to facilitate comparison with histograms corresponding to the whole cubes. As expected, the plots of the three thirds show the same tendency as observed in Figs. 16 and 17, where a damage concentration at the external part of the cubes, from $d = 0.9$ onwards, was observed. Nevertheless, it is larger as we approach the bottom third of the specimens, although the damage, as h varies, remains constant, as we will see in the following subsection. Note that the spherical seat of the machine is placed at the upper steel platen (see Fig. 4), which may cause the damage in the section to be closer to the randomly-distributed one.

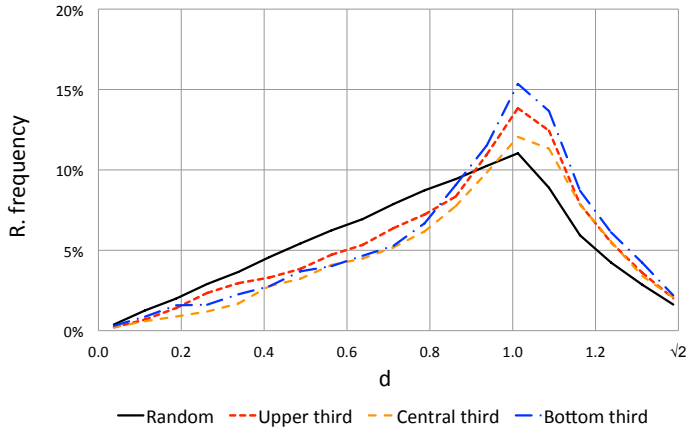

Figure 20: Summed mean histogram in the h direction of the Monotonic series. Comparison in height.

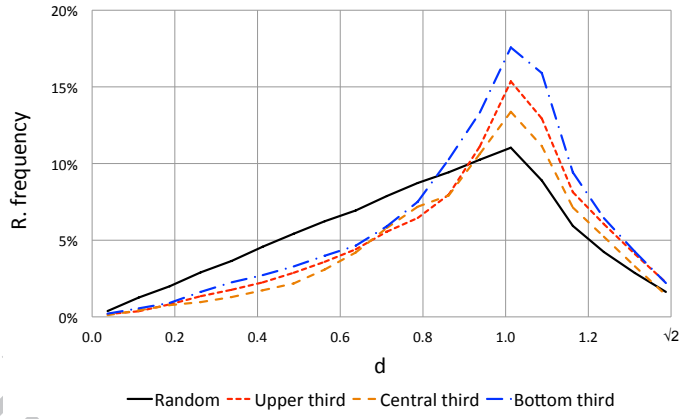

Figure 21: Summed mean histogram in the h direction of the Cyclic series. Comparison in height.

These differences in damage concentration along the height of the cubes can also be verified in the original images obtained by the CT-Scan for the monotonically-loaded specimens, Fig.22, and for the cyclically-loaded specimens, Fig.23. The upper third of the specimen, which was in contact with the platen equipped with the spherical seat, shows a more uniform distribution of cracks, see Figs. 22a and 23a, while the bottom third of the specimen, where

the platen is fixed, shows cracks especially concentrated in the external half of the cubes, see Figs. 22c and 23c.

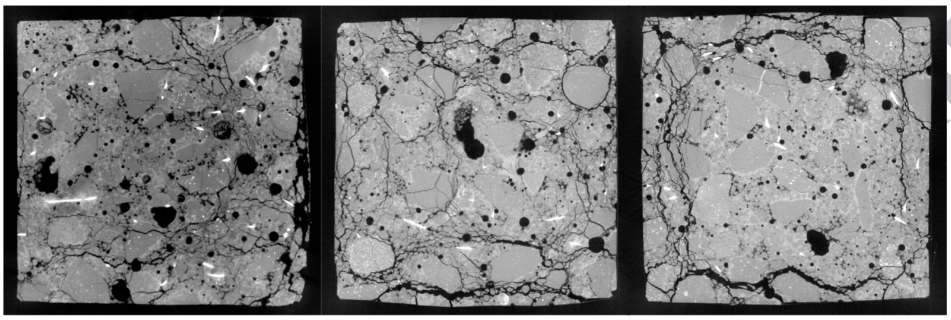

(a) (b) (c)

Figure 22: Damage comparison in height of a monotonically-loaded specimen. (a) Upper third, (b) central third and (c) bottom third.

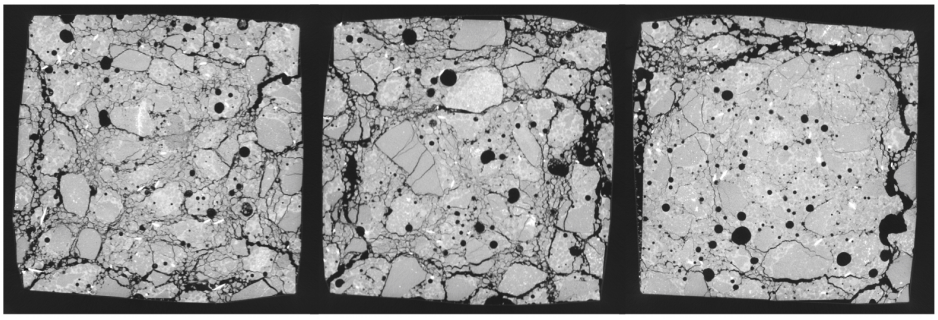

(a) (b) (c)

Figure 23: Damage comparison in height of a cyclically-loaded specimen. (a) Upper third, (b) central third and (c) bottom third.

The CT-Scan technology reveals that the cracking in the specimens varies along the height of the specimen, which could be linked to the boundary conditions of the tests. Both monotonic and cyclic tests, performed in a servo-hydraulic machine equipped with a single spherical seat, result in a non-uniform distribution of the cracks along the height of the specimens. This concurs with the findings of del Viso *et al.* [44], who tested cubic and cylindrical specimens

on a compressive setup. They plotted the crack patterns of the specimens of the two shapes and several sizes, after a simple visual inspection. They concluded that the extent of cracking throughout the specimens depended on their shape. In fact, it was denser in the cubes than in the cylinders. Moreover, they showed that there was a significant crack dispersion in the upper part of their cubes, which was also loaded through a spherical seat. Furthermore, they noted that the fracture process in the cubes was a consequence of a stress concentration near the cube corners which produced crushing and vertical cracks that might end-up forming column-like corners. The non-uniform distribution of cracks following from the boundary conditions may also explain why is it that fatigue results depend on the uncertainty of the loading eccentricity, as recently stated by Tarifa *et al.* [40].

3.4. Summed histograms along the d direction

The representation of summed histograms in the d direction allows analyzing the damage of the specimens according to their height. We obtained flat histograms, which represent the relative frequencies of empty voxels along the h coordinate, in parallel to the load direction.

The summed histograms in the d direction are represented in Fig. 24 for the monotonic series and Fig. 25 for the cyclic series. In the plots, the solid red line shows the mean values obtained from the scanned specimens. As previously observed, all the cases were compared with the randomly-distributed curve in black. In addition, the plots include the confidence interval of 90%. Therefore, the relative frequency is similar along the height of the monotonically-loaded and cyclically-loaded specimens, and they follow a random defect distribution. Thus, the extent of damage is similar at any height, although as we already have observed in the previous subsection, the damage is uniformly distributed at the upper part of the cube whereas it concentrates close to the surface at the bottom, which is in contact with the fixed platen.

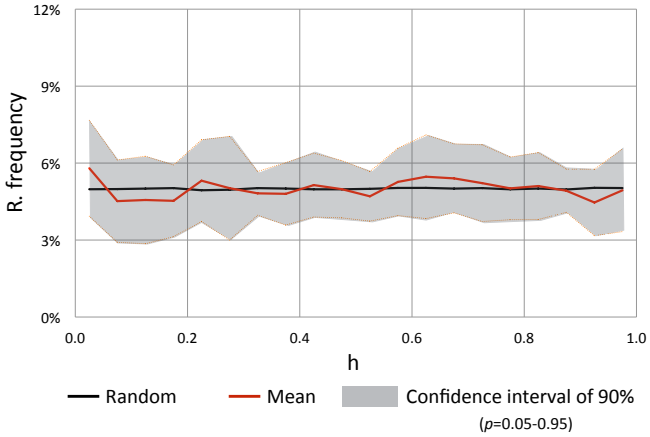

Figure 24: Summed histogram in the d direction. Monotonic series.

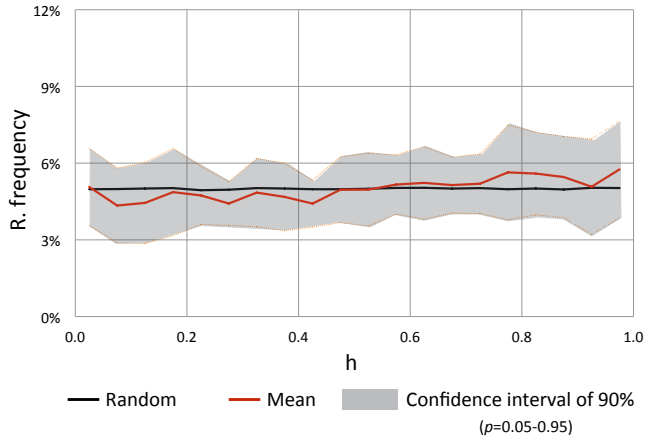

Figure 25: Summed histogram in the d direction. Cyclic series.

4. Conclusions

385 The CT-Scan with specific post-processing software is a powerful tool to measure the internal damage of concrete and fiber-reinforced concrete specimens. In this work we used it to verify whether monotonic loading can be considered a limit case of fatigue loading, as it is axiomatically assumed by researchers in the fatigue of these materials. Naked-eye comparison of crack patterns generated

by both types of loading usually leads to the conclusion that this assumption is correct. Still, the extension of the damage propagation or even some fracture mechanisms could vary with the type of loading. Furthermore, it is not evident that the extension of the cracking should be commensurate in both cases. These damage processes could leave a trace in the internal cracking pattern and thus they could be studied by a CT-Scan and a data processing technique.

The material used in the study was a self-compacting steel fiber-reinforced concrete. Four series of 40 mm-edged cubes were prepared. One of them, comprised of 15 cubes, was used to obtain the average compressive strength. Eight cubes forming another series were tested under monotonic loading whereas 16 cubes were tested in low cycle fatigue loading, which comprised the monotonic and cyclic series respectively. Finally, another 8 cubes were kept intact so as to study the original fiber and pore distribution in the specimens. All the cubes of the latter three series were scanned to obtain their internal void distribution. Additionally, the intact series was used to study the fiber distribution and orientation; it was found that fibers are uniformly distributed but tend to lay horizontally with no preferential direction. As cubes were always loaded along the casting direction (vertical axis), it was concluded that there should not be significant differences among their crack patterns due to variations in the distribution and orientation of fibers among cubes.

The images were processed with a novel methodology, especially developed by the authors for this research (named *circumferential test*); it consists in summing the voxels representing voids along the height or along circumferences around the central axis, i.e. the loading direction, to generate average histograms that allow quantitative comparison among them.

The study of the specimens transversal to the load direction shows that the voids of the intact specimens are randomly-distributed. On the contrary, the cracks of the tested specimens are not randomly-distributed, but they are rather concentrated on the external part of the cubes. Furthermore, the specimens tested under monotonic loading show, from a statistical point of view, the same crack pattern as the specimens tested under cyclic loading. In other words, 3D

cracking patterns and corresponding volume generated in fiber-reinforced cubes monotonically tested in compression have the same average features and are commensurate with these of the same type of cubes but tested in fatigue. This demonstrates that internal micro-mechanisms of failure (crack nucleation and growth, crack distribution, etc.) due to monotonic static compressive tests are almost identical to the ones generated by low-cycle fatigue tests and, so, this confirms the hypothesis of convergence to the initial distribution, which assumes that compressive tests are a limit case of a cyclic test where failure is achieved in the first cycle.

In addition, the transversal histograms were summed into three different thirds in height, which may reveal the effect of the boundary conditions of the tests in the crack pattern. Both histograms and direct images from the CT-Scan exhibit a non-uniform distribution of cracks along the height of the specimens. In the upper third of the cubes, close to the machine platen equipped with the spherical seat, the crack distribution is basically uniform, whereas in the bottom third, where the platen is fixed, the cracks are concentrated at the external part of the cube, close to the surfaces. However, the relative frequencies along the height remain constant.

It should be emphasized that our conclusions are drawn from the tests in the paper and, thus, they limited to steel fiber-reinforced concrete under low cycle fatigue. However, Poveda et al. [38] concluded that fatigue failure mainly depends on the concrete matrix, although fibers may modify the fatigue life in some conditions; thus, there is some evidence that the conclusions drawn here could be extended to plain concrete in case fatigue life correlates with the crack pattern, although additional experimental proof for that should be provided. Similarly, the cyclic-loading parameters or the choice of specimen could have some influence on the crack patterns and, consequently, it would be necessary to check that there is convergence to the initial distribution for some other cases.

5. Acknowledgements

The authors are grateful for the financial support from the *Ministerio de Economía y Competitividad*, BIA2015-68678-C2-R, Spain. Access to the CT-Scan of the *Centro Nacional de Investigación sobre la Evolución Humana*, Burgos, Spain, is likewise appreciated.

[1] K. Aas-Jackobsen, Fatigue of concrete beams and columns, Doctoral thesis, University of Trondheim (1970).

[2] R. Tepfers, T. Kutti, Fatigue strength of plain, ordinary and lightweight concrete, Journal of the American Concrete Institute 76 (5) (1979) 635–652.

[3] B. Zhang, D. V. Phillips, K. Wu, Effects of loading frequency and stress reversal on fatigue life of plain concrete, Magazine of Concrete Research 48 (4) (1996) 292–305. doi:10.1680/macr.1996.48.177.361.

[4] T. Hsu, Fatigue of plain concrete, Journal of the American Concrete Institute 78 (4) (1981) 192–305.

[5] G. Petkovic, R. Lenschow, H. Stemland, S. Rosseland, Fatigue of high-strength concrete, ACI Special Publication 121 (25) (1990) 505–525.

[6] D. F. Zhao, Q. Y. Chang, J. H. Yang, Y. P. Song, A new model for fatigue life distribution of concrete, Key Engineering Materials 348-349 (2007) 201–204. doi:10.4028/www.scientific.net/KEM.348-349.201.

[7] C. Przybilla, A. Fernández-Cantelli, E. Castillo, Deriving the primary cumulative distributive function of fracture stress for brittle materials from 3- and 4-point bending tests, Journal of the European Ceramic Society 31 (2011) 451–460. doi:10.1016/j.jeurceramsoc.2010.11.007.

[8] L. Saucedo, R. C. Yu, A. Medeiros, X. X. Zhang, G. Ruiz, A probabilistic fatigue model based on the initial distribution to consider frequency effect in plain and fiber reinforced concrete, International Journal of Fatigue 48 (2013) 308–318. doi:10.1016/j.ijfatigue.2012.11.013.

[9] T. Longbiao, Fatigue damage and lifetime of SiC/SiC Ceramic-matrix composite under cyclic loading at elevated temperatures, Materials 10 (2017) 371. doi:10.3390/ma10040371.

[10] A. Chandrappa, K. Biligiri, Flexural-fatigue characteristics of pervious concrete: Statistical distributions and model development, Construction and Building Materials 153 (2017) 1–15. doi:10.1016/j.conbuildmat.2017.07.081.

[11] L. Longbiao, Fatigue life prediction of carbon fiber-reinforced ceramic-matrix composites at room and elevated temperatures. Part II: Experimental comparison, Applied Composite Materials 22 (2015) 961–972. doi:10.1007/s10443-015-9445-4.

[12] P. Suthiwarapirak, T. Matsumoto, T. Kanda, Flexural fatigue failure characteristics of an engineered cementitious composite and polymer cement mortar, J. Materials, Conc. Struct. Pavements 718(57) (2002) 121–134. doi:10.2208/jscej.2002.718_121.

[13] M. Pindado, A. Aguado, A. Josa, Fatigue behavior of polymer-modified porous concretes, Cement and Concrete Research 29(7) (1999) 1077–1083. doi:10.1016/S0008-8846(99)00095-2.

[14] J. Zhang, H. Stang, V. Li, Fatigue life prediction of fiber reinforced concrete under flexural load, International Journal of Fatigue 21(10) (1999) 1033–1049. doi:10.1016/S0142-1123(99)00093-6.

[15] H. Sharma, A. Swamy, Development of probabilistic fatigue curve for asphalt concrete based on viscoelastic continuum damage mechanics, International Journal of Pavement Research and Technology 9(4) (2016) 270–279. doi:10.1016/j.ijprt.2016.07.004.

[16] E. Castillo, A. Fernández-Canteli, A Unified Statistical Methodology for Modeling Fatigue Damage, Springer Netherlands, 2009, ISBN: 978-1-4020-9182-7.

[17] Model Code 2010, Final draft. FIB Bulletin, EPFL Lausanne (2012).

[18] Eurocode 2, Design of Concrete Structures. European Committee for Standardization. EN 1992-2:2005/AC:2008. European Standards. Brussels, Belgium (2008).

[19] J. Schnell, K. Schladitz, F. Schuler, Richtungsanalyse von Fasern in Betonen auf Basis der Computer-Tomographie [in German]. Direction analysis of fibers in concrete on basis of computed tomography, Beton Stahlbetonbau 105 (2) (2010) 72–77. doi:10.1002/best.200900055.

[20] G. Pittino, G. Geier, L. Fritz, M. Hadwiger, J. Rosc, T. Pabel, Computertomografische Untersuchung von Stahlfaserspritzbeton mit mehrdimensionalen Transferfunktionen [in German]. Computer tomographic investigation of steel fiber reinforced sprayed concrete using multidimensional transfer functions, Beton Stahlbetonbau 106 (6) (2011) 364–370.

[21] M. Krause, J. M. Hausherr, B. Burgeth, C. Herrmann, W. Krenkel, Determination of the fibre orientation in composites using the structure tensor and local X-ray transform, Journal of Material Science 45 (2010) 888–896. doi:10.1007/s10853-009-4016-4.

[22] J.-P. Suuronen, A. Kallonen, K. Eik, J. Puttonen, R. Serimaa, H. Herrmann, Analysis of short fibres orientation in steel fibre-reinforced concrete (SFRC) by X-ray tomography, Journal of Material Science 48 (2013) 1358–1367. doi:10.1007/s10853-012-6882-4.

[23] M. A. Vicente, D. C. González, J. Mínguez, Determination of dominant fibre orientations in fibre-reinforced high-strength concrete elements based on computed tomography scans, Nondestructive Testing and Evaluation 29 (2) (2014) 164–182. doi:10.1080/10589759.2014.914204.

[24] A. C. Bordelon, J. R. Roesler, Spatial distribution of synthetic fibers in concrete with X-ray computed tomography, Cement and Concrete Composites 53 (2014) 35–43. doi:10.1016/j.cemconcomp.2014.04.007.

[25] H. Herrmann, E. Pastorelli, A. Kallonen, J. P. Suuronen, Methods for fibre orientation analysis of X-ray tomography images of steel fibre reinforced concrete (SFRC), Journal of Materials Science 51 (8) (2016) 3772–3783. doi:10.1007/s10853-015-9695-4.

[26] J. Mínguez, D. C. González, M. A. Vicente, Fiber geometrical parameters of fiber-reinforced high strength concrete and their influence on the residual post-peak flexural tensile strength, Construction and Building Materials 168 (2018) 906–922. doi:10.1016/j.conbuildmat.2018.02.095.

[27] J. Mínguez, D. C. González, M. A. Vicente, Influence of fibre volume fraction and fibre orientation on the residual flexural tensile strength of fibre-reinforced concrete, Hormigón y Acero. In Press. doi:10.1016/j.hya.2017.05.007.

[28] T. Suzuki, H. Ogata, R. Takada, M. Aoki, M. Ohtsu, Use of acoustic emission and X-ray computed tomography for damage evaluation of freeze-thawed concrete, Construction and Building Materials 24 (12) (2010) 2347–2352. doi:10.1016/j.conbuildmat.2010.05.005.

[29] J. Yuan, Y. Liu, H. Li, B. Zhang, Experimental Investigation of the variation of concrete pores under the action of freeze-thaw cycles by using X-ray CT, Advances in Materials Science and Engineering 2014. doi:10.1155/2014/571357.

[30] M. Vicente, D. González, J. Mínguez, M. Tarifa, G. Ruiz, R. Hindi, Influence of the pore morphology of high strength concrete on its fatigue life, International Journal of Fatigue 112 (2018) 106–116. doi:10.1016/j.ijfatigue.2018.03.006.

[31] H. Lu, K. Peterson, O. Chernoloz, Measurement of entrained air-void parameters in Portland cement concrete using micro X-ray computed tomography, International Journal of Pavement Engineering 19(2) (2018) 109–121. doi:10.1080/10298436.2016.1172705.

[32] Y.-S. Wang, J.-G. Dai, X-ray computed tomography for pore-related characterization and simulation of cement mortar matrix, NDT&E International 86 (2017) 28–35. doi:10.1016/j.ndteint.2016.11.005.

[33] M. Moradian, Q. Hu, M. Aboustait, M. Ley, J. Hanan, X. Xiao, G. Scherer, Z. Zhang, Direct observation of void evolution during cement hydration, Materials and Design 136 (2017) 137–149. doi:10.1016/j.matdes.2017.09.056.

[34] H. Lu, E. Alymov, S. Shah, K. Peterson, Measurement of air void system in lightweight concrete by X-ray computed tomography, Construction and Building Materials 152 (2017) 467–483. doi:10.1016/j.conbuildmat.2017.06.180.

[35] K. Kim, T. Yun, J. Choo, D. Kang, H. Shin, Determination of air-void parameters of hardened cement-based materials using X-ray computed tomography, Construction and Building Materials 37 (2012) 93–101. doi:10.1016/j.conbuildmat.2012.07.012.

[36] M. A. Vicente, J. Mínguez, D. C. González, Book Chapter: The Use of Computed Tomography to Explore the Microstructure of Materials in Civil Engineering: From Rocks to Concrete, in: A. M. Halefoglu (Ed.), Computed Tomography - Advanced Applications, InTech, 2017, pp. 207–230.

[37] A. Medeiros, X. Zhang, G. Ruiz, R. Yu, M. S. L. Velasco, Effect of the loading frequency on the compressive fatigue behavior of plain and fiber reinforced concrete, International Journal of Fatigue 70 (2015) 342–350. doi:10.1016/j.ijfatigue.2014.08.005.

[38] E. Poveda, G. Ruiz, H. Cifuentes, R. C. Yu, X. X. Zhang, Influence of the fiber content on the compressive low-cycle fatigue behavior of self-compacting SFRC, International Journal of Fatigue 101(1) (2017) 9–17. doi:10.1016/j.ijfatigue.2017.04.005.

[39] T. Ponikiewski, J. Golaszewski, Properties of steel fibre reinforced self-compacting concrete for optimal rheological and mechanical properties in precast beams, Procedia Engineering 65 (2013) 290–295. doi:10.1016/j.proeng.2013.09.045.

[40] M. Tarifa, G. Ruiz, E. Poveda, X. X. Zhang, M. A. Vicente, D. C. González, Effect of uncertainty on load position in the fatigue life of steel-fiber reinforced concrete under compression, Materials and Structures 51:31 (2018) 1–11. doi:10.1617/s11527-018-1155-6.

[41] J. Ortega, G. Ruiz, R. C. Yu, N. Afanador-García, M. Tarifa, E. Poveda, X. Zhang, F. Evangelista, Number of tests and corresponding error in fatigue of concrete, International Journal of Fatigue. Submitted.

[42] EN 12390-13, Testing hardened concrete. Part 13: Determination of secant modulus of elasticity in compression (2012).

[43] S. Greenland, S. J. Senn, K. J. Rothman, J. B. Carlin, C. Poole, S. N. Goodman, D. G. Altman, Statistical tests, P values, confidence intervals, and power: A guide to misinterpretations, European Journal of Epidemiology 31 (2016) 337–350. doi:10.1007/s10654-016-0149-3.

[44] J. R. del Viso, J. R. Carmona, G. Ruiz, Shape and size effects on the compressive strength of high-strength concrete, Cement and Concrete Research 38 (2008) 386–395. doi:10.1016/j.cemconres.2007.09.020.

The paper develops an image processing technique to analyze the fracture patterns of steel fiber-reinforced concrete specimens subjected to monotonic and to fatigue loading.

It is applied to show that the crack patterns of monotonically and cyclically-tested specimens are undistinguishable from each other in the average.

The technique includes a novel algorithm to statistically resolve between 3D cracking patterns of a series of tested specimens.

A study on the fiber distribution and orientation is also included.